INTERNATIONAL JOURNAL FOR NUMERICAL METHODS IN FLUIDS
*Int. J. Numer. Meth. Fluids* 2007; **53**:651–667
Published online 23 August 2006 in Wiley InterScience (www.interscience.wiley.com). DOI: 10.1002/fld.1302

# Adaptive wall functions for the $v^2$-$f$ turbulence model

Georgi Kalitzin*,† and Gorazd Medic‡

*Mechanical Engineering Department, Stanford University, Stanford, CA 94305, U.S.A.*

SUMMARY

Adaptive wall functions for the $v^2$-$f$ turbulence model have been derived for the flow over a flat plate at zero pressure gradient. These wall functions were implemented via tables for the turbulence quantities and the friction velocity $u_\tau$. A special treatment for the $\varepsilon$ and $f$ boundary conditions is proposed. On fine grids ($y^+<1$) this approach yields results consistent with the wall integration solution. Detailed numerical results are presented for a zero pressure gradient boundary layer and separated flow over a ramp. Copyright © 2006 John Wiley & Sons, Ltd.

Received 24 February 2006; Revised 24 May 2006; Accepted 26 May 2006

KEY WORDS: RANS; $v^2$-$f$ model; wall functions

## 1. INTRODUCTION

Wall functions for RANS were first developed using the universal character of the logarithmic layer for the design of off-wall boundary conditions [1]. These boundary conditions require the first cell centre to lie in the logarithmic layer and their application to the intermediate (buffer) layer or viscous sub-layer is usually inaccurate. Adaptive wall function formulations that do not restrict the location of the first grid point between wall and logarithmic layer have become the focus of considerable amount of research and are widely used in computational codes.

In Reference [2], we have proposed an efficient, accurate and robust approach for adaptive wall functions that is applicable to different RANS turbulence models. The proposed wall functions are formulated for zero pressure gradient flows. They are based on look-up tables for the

*Correspondence to: Georgi Kalitzin, 488 Escondido Mall, Building 500, Room 500V, Mechanical Engineering Department, Stanford University, Stanford, CA 94305-3030, U.S.A.
†E-mail: kalitzin@stanford.edu
‡E-mail: gmedic@stanford.edu

Contract/grant sponsor: Department of Energy
Contract/grant sponsor: General Electric Aircraft Engines

turbulence quantities and the friction velocity $u_\tau = \sqrt{\nu\, \mathrm{d}u/\mathrm{d}y|_w}$. These tables are built upon well-resolved, grid-converged numerical solutions obtained with the particular turbulence model. The boundary conditions derived from these tables are valid for the viscous, logarithmic as well as the intermediate region. The friction velocity $u_\tau$ is computed explicitly avoiding a costly iterative method.

The adaptive wall functions were validated for the flow over a flat plate. Detailed analysis of the discrepancy between the coarse grid wall function solutions and the corresponding wall integration was performed. A method that allows the isolation of the errors resulting from the modelling of the physics was proposed. It is based on a computational grid that is identical to the wall integration grid but shifted by a distance $\delta$ from the wall. This practically eliminates the numerical errors caused by the coarseness of the wall functions grid in the near-wall region. Indeed, this method confirms the validity of the proposed boundary conditions based on look-up tables; i.e. the discrepancies on the coarse grid are a consequence of numerical errors.

The adaptive wall functions have also been applied to recirculating flow. It has been observed that for the $v^2$-$f$ model [3] the scaling used to build the look-up tables breaks down at separation and reattachment points where $u_\tau \to 0$. In the present paper, we investigate that problem in detail and propose a new formulation for wall functions which on fine grids ($y^+ < 1$) yields results consistent with the wall integration solution. These new wall functions are applied to flow over a ramp that includes a recirculation region.

## 2. ADAPTIVE WALL FUNCTIONS

In the case of turbulent flow of incompressible fluid with constant molecular viscosity, the boundary layer can be split in three distinct regions: the viscous sublayer, the logarithmic layer and the defect layer. The location of the outer edge of the logarithmic layer depends on the Reynolds number, i.e. the extent of the logarithmic layer grows with increasing Reynolds number. In a quasi-equilibrium boundary layer (e.g. flow over a flat plate at zero pressure gradient), the region between the wall and the outer edge of the logarithmic layer is universal; i.e. the velocity profiles collapse when scaled with the friction velocity $u_\tau$ and molecular viscosity $\nu$. The equations are recast in non-dimensional form; the velocity and turbulence variables in plus units are:

$$U^+ = \frac{U}{u_\tau}, \quad y^+ = \frac{y u_\tau}{\nu}, \quad \nu_t^+ = \frac{\nu_t}{\nu}, \quad k^+ = \frac{k}{u_\tau^2}, \quad \varepsilon^+ = \frac{\varepsilon \nu}{u_\tau^4}, \quad \overline{v^2}^+ = \frac{\overline{v^2}}{u_\tau^2}, \quad f^+ = \frac{f\nu}{u_\tau^2} \tag{1}$$

The universal function $U^+(y^+)$ is obtained for each model by solving the wall layer equations numerically. Note that $U$ represents the wall-tangential velocity component. Now, knowing the universal function, the friction velocity can be solved from the computed velocity at the first grid point. The velocity profile, $U^+(y^+)$, is transformed to $U^+(y^+ \cdot U^+) = U^+(Re)$, where $Re = yU/\nu$. This transformation can be done once and for all, and the function stored in a table. Using $y_1$ and $U_1$, where index 1 denotes the wall adjacent cell centre, this look-up table provides $U_1^+$. The friction velocity follows as $u_\tau = U_1/U_1^+$. This eliminates the need for costly iterative computation of $u_\tau$.



DOI: 10.1002/fld

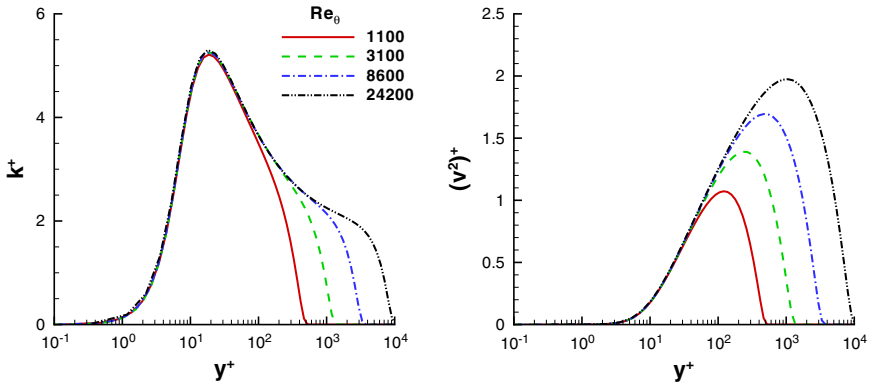


Figure 1. Numerical solution for $v^2$-$f$ model at different $Re_\theta$: $k^+$ and $\overline{v^2}^+$.

The eddy-viscosity is explicitly related to the velocity profile, i.e. in the entire region between the wall and the outer edge of the logarithmic boundary layer the equation $(1+v_t^+)\mathrm{d}U^+/\mathrm{d}y^+=1$ holds. In some wall function formulations the velocity profile and eddy-viscosity do not obey this relation. The result is grid dependence.

In the present paper, this is addressed by generating a look-up table for each non-dimensionalized turbulence variable from a well-resolved numerical solution for the $v^2$-$f$ model. Each turbulence variable is tabulated against $y^+$ and the table takes the form of spline coefficients (see Appendix B). It is possible to create such tables for the $v^2$-$f$ model because the numerical solution shows universal character. This is shown for the turbulent kinetic energy $k^+$ and the scalar $\overline{v^2}^+$ in Figure 1 for different $Re_\theta$.

### 2.1. *Numerical implementation*

The adaptive wall functions have been implemented in two three-dimensional, cell centred RANS flow solvers: a single-block, Cartesian, incompressible solver IBRANS [4] and a multi-block, body-fitted, compressible solver SUmb [5].

In the Cartesian flow solver, the $x$-velocity component, $U$, is tangential to the wall and the wall function tables (see Appendix B) are used in the following way. First, the velocity $U_1$ and wall distance $y_1$ for wall adjacent cell centre are used to compute a corresponding Reynolds number $Re_1=y_1^+U_1^+=y_1U_1/\nu$. The non-dimensional velocity is obtained from the table: $U_1^+=U^+(Re_1)$ and the friction velocity follows to: $u_\tau=U_1/U_1^+$. The viscous flux at the wall, $\nu\,\mathrm{d}U/\mathrm{d}y$, is substituted with $u_\tau^2$ when solving the momentum equation. The turbulence variables are enforced in the cell centre of the wall adjacent cells. First the non-dimensional wall distance $y_1^+=y_1u_\tau/\nu$ is computed. The tables provide the turbulence variable, say $k_1=k_1^+u_\tau^2$. This value is used as a boundary condition, i.e. the turbulence field equations are not solved in the wall adjacent cells. IBRANS solves the mean flow and turbulence equation implicitly. Wall function computations require an appropriate modification of the implicit matrices. When solving the mean flow equation, the implicit matrix for the $U$-momentum equation is discretized in the same way as when using no slip boundary conditions. The wall function flux is incorporated into the right hand side (RHS) as a correction. When solving the turbulence equation, the diagonal and



DOI: 10.1002/fld

off-diagonal elements for the wall adjacent cells in the implicit matrix are set to one and zero, respectively.

SUmb has been recently developed at Stanford under the Department of Energy's (DoE) Advanced Simulation and Computing (ASC) program. It is a state-of-the-art multiblock flow solver, based on a finite-volume formulation, a modified Runge–Kutta time integration scheme, a Roe upwind spatial discretization and a multigrid solution procedure to accelerate convergence to a steady state. The wall function implementation has been adjusted for SUmb which is an explicit and curvilinear code. To account for the latter, the stress tensor and velocity vector in the wall adjacent cells is computed and then rotated to a local wall aligned coordinate system. The shear stress is then substituted with the square of the friction velocity that is obtained from the look-up table using the tangential velocity component, as discussed before. Finally, the modified stress tensor is rotated back to the global coordinate system.

The results for the flat plate and the recirculating flow via suction and blowing are computed with the IBRANS solver. SUmb has been used for the flow over a ramp. If not specified otherwise, the $v^2$-$f$ model with $N=6$ has been used in the computations (for more details on the $v^2$-$f$ model see Appendix A).

## 3. FLOW OVER A FLAT PLATE

Wall functions are designed to be used with coarse near-wall grids. The solution of the discrete RANS equations is associated with a numerical error that increases with decreasing grid resolution. The difficulty in testing wall function implementations is to distinguish between this numerical error and inaccuracies that may result from the physical model (boundary condition). The $\delta$-grid method eliminates the numerical error and provides a test for the correctness of the applied boundary condition. In the $\delta$-grid, a wall integration grid is shifted by a distance $\delta$ into the flow to provide the desired $y^+$ location of the first cell. The wall functions provide the desired boundary conditions. At the same time, the grid resolution and the associated numerical error is of the same order as for the wall integration.

In Figures 2 and 3, flow over a flat plate is solved up to the location defined by momentum thickness based Reynolds number of $Re_\theta = 7700$. The first cell centre at the inflow is at $y_1^+ = 0.11, 1.1, 2.5, 5, 11, 25, 111$. When $\delta$-grids are used with the correct boundary conditions, the computations collapse onto the wall integration profile; the results for the velocity $U^+$, eddy-viscosity $v_t^+$ and the turbulence variables $k^+$, $\overline{v^2}^+$, $\varepsilon^+$ and $f^+$ are presented in Figure 2. Since the results for all the grids are practically coinciding, the colors of the curves are chosen to alternate between grey and black to visualize the first grid point for each grid. The results obtained on "classic" coarse grids with the same $y_1^+$ values are presented in Figure 3. The spread in the results is the consequence of numerical errors. This is inferred from the fact that solutions on the $\delta$-grids collapse on the wall integration result.

The spread of the $U^+$ profiles in the defect region is a result of different predictions for $u_\tau$ which, in turn, affects the skin friction prediction. The computation with the first cell centre at $y^+ = 5$ or $y^+ = 11$ under-predicts and the computation with $y^+ = 111$ over-predicts the non-dimensional velocity profile when compared with the wall integration solution. The deviation of the eddy-viscosity $v_t^+$ for grids with the first cell centre at $y^+ = 25$ or $y^+ = 111$ can be explained by the relative coarseness of those grids throughout the boundary layer.



DOI: 10.1002/fld

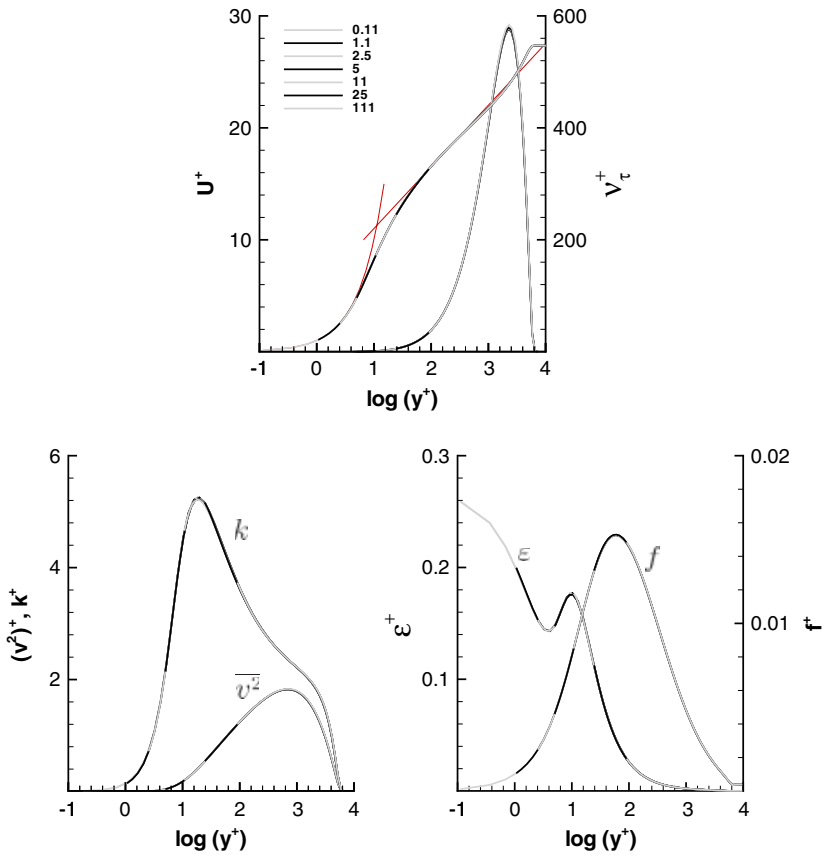


Figure 2. Application of adaptive wall functions using $\delta$-grids.

## 4. BOUNDARY CONDITIONS FOR $\varepsilon$ AND $f$

### *4.1. Boundary condition for $\varepsilon$*

The ability of these wall functions to capture pressure gradient driven separation and reattachment has been studied in Reference [2] by considering a simple test problem: the boundary layer over a flat plate with an imposed streamwise pressure gradient. The pressure gradient was modulated by suction and blowing along the upper boundary of the computational domain. Contours of turbulent kinetic energy $k$ and streamlines computed using wall integration are shown in Figure 4.

As pointed out in Reference [2], the scaling used to build the look-up table wall functions for the $v^2$-$f$ model breaks down when separation is present. On the fine grid ($y_1^+ = 1$ at inlet) the skin friction computed with wall functions that use $\varepsilon$ from the look-up table differs from the wall integration solution as shown in Figure 5.

This is related to the non-zero, finite boundary condition for $\varepsilon$ and its scaling with $u_\tau$. In the wall function approach based on look-up tables, $\varepsilon_1$ in the first cell centre is computed from $\varepsilon^+_{\text{table}}$ which is approximately 0.26. However, when wall integration is used, $\varepsilon^+$ becomes singular near



DOI: 10.1002/fld

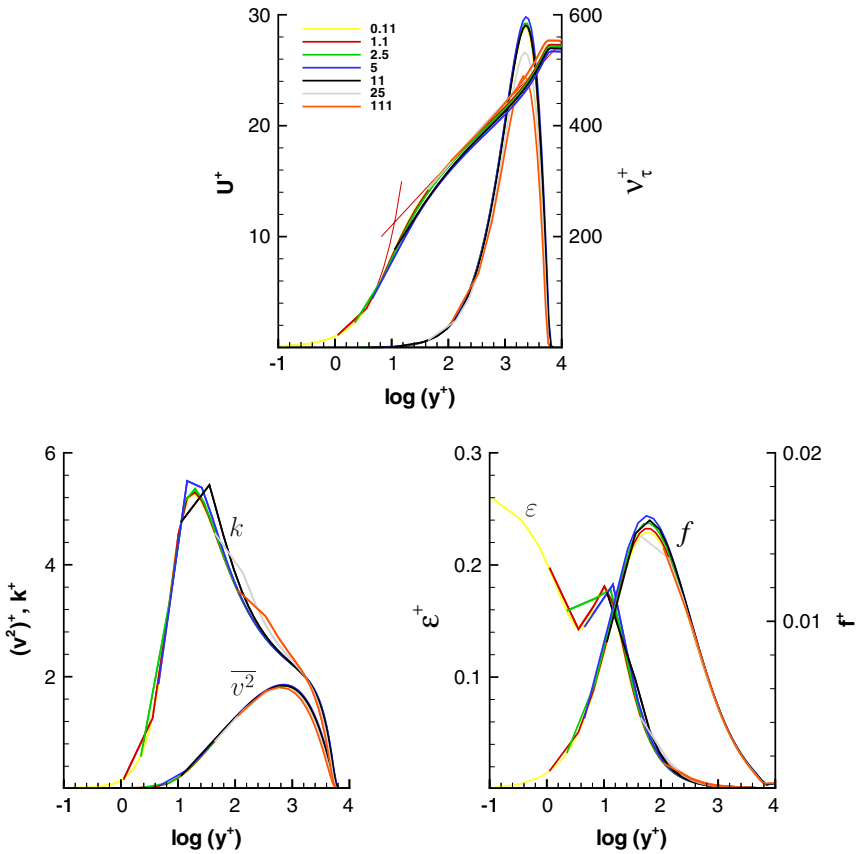


Figure 3. Application of adaptive wall functions using coarse grids.

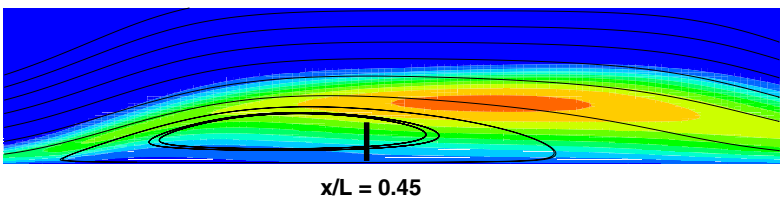


Figure 4. $k$ contours computed using $v^2$-$f$ model, wall integration.

the separation and reattachment points where $u_\tau$ approaches zero; $\varepsilon$ in the wall integration approach has a finite value at those points as shown in Figure 6.

This problem can be solved by avoiding the use of a table for $\varepsilon^+$. In analogy to the derivation of the wall integration boundary condition for $\varepsilon_w$ in Reference [3], an equation for $\varepsilon$ in the first cell centre above the wall can be derived for coarse grids. Using the usual boundary layer assumption that the turbulence quantities depend only on the distance to the wall and neglecting



DOI: 10.1002/fld

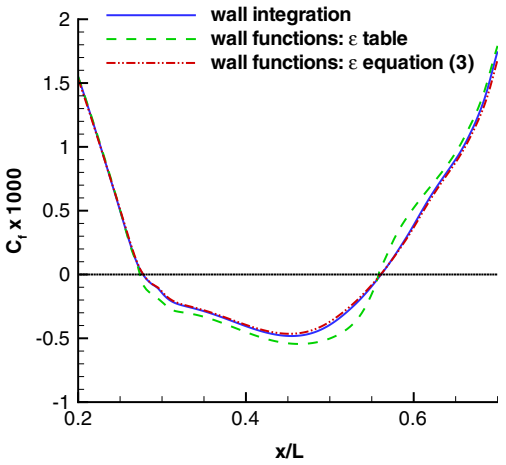


Figure 5. Skin friction computed on the fine grid with $y_1^+ = 1$ at inlet.

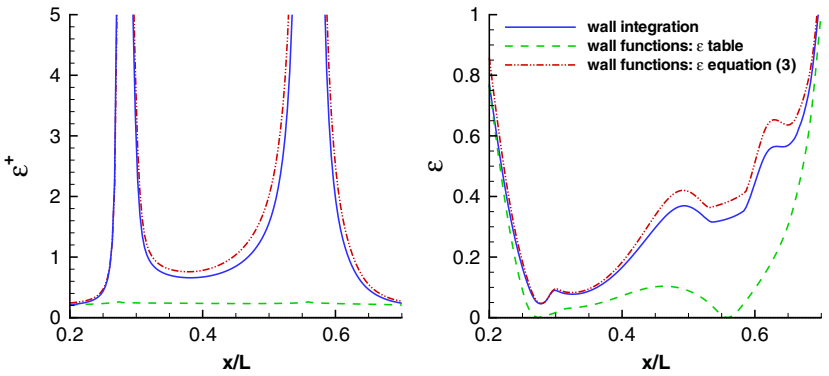


Figure 6. $\varepsilon^+$ and $\varepsilon$ in the first cell above the wall.

the convection terms, the $k$-equation can be simplified for the region between wall and outer edge of the logarithmic layer as

$$\varepsilon = P_k + \frac{\mathrm{d}}{\mathrm{d}y}\left((v + v_t)\frac{\mathrm{d}k}{\mathrm{d}y}\right) \tag{2}$$

In discrete form (for notation see Figure 7), using a finite difference method, Equation (2) can be written as (with $\mathrm{d}k/\mathrm{d}y = 0$ at the wall):

$$\varepsilon_1 = P_{k1} + \frac{1}{y_{12}}\left((v + v_t)_{12}\frac{(k_2 - k_1)}{y_2 - y_1}\right) \tag{3}$$

where $P_{k1} = v_{t1}(\mathrm{d}U/\mathrm{d}y)_1^2$. The look-up table is used to compute $(\mathrm{d}U/\mathrm{d}y)_1$ and $k_1$.



DOI: 10.1002/fld

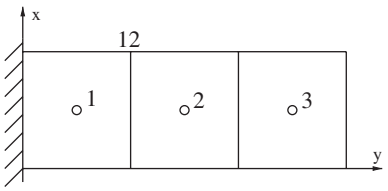


Figure 7. Sketch of near-wall grid with notation.

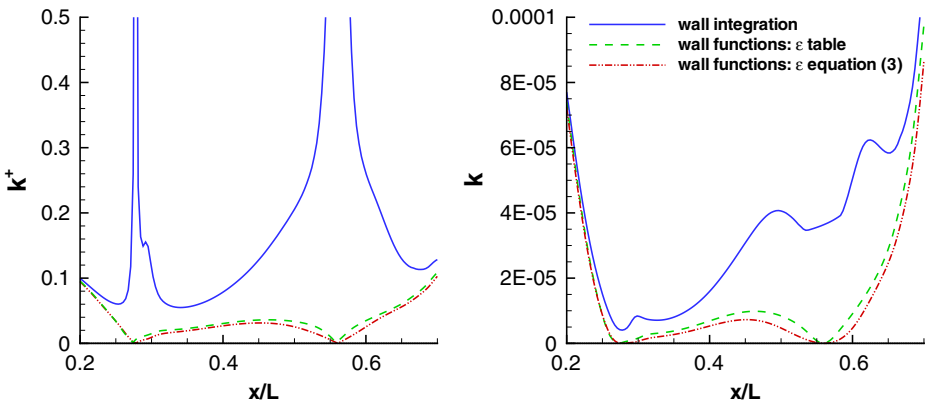


Figure 8. $k^+$ and $k$ in the first cell above the wall.

The effect of using this boundary condition for $\varepsilon$ can be seen in Figure 6. When Equation (3) is used, $\varepsilon$ approaches the wall integration solution. On the other hand, when the look-up table is used for $\varepsilon^+$, $\varepsilon$ is proportional to $u_\tau$. This affects the skin friction as shown in Figure 5. The wall integration solution and the wall function solution using Equation (3) practically coincide.

A closer look at the turbulent kinetic energy reveals a similar problem: $k$ computed using wall integration does not scale with $u_\tau$ as shown in Figure 8. Obviously, the modification for $\varepsilon$ proposed above does not eliminate this problem. However, the error for $k$ in the first cell above the wall is less significant. It impacts the diffusion term in the adjacent cell which on a uniform grid has the form: $\nu(2k_2 - k_1 - k_3)/\Delta y^2$. The value of $k$ in the first cell is very small and it grows rapidly with increasing distance from the wall; an error in $k_1$ has a small impact on the diffusion term in the second cell above the wall as the difference between $k_2$ and $k_3$ dominates this term. In contrast, $\varepsilon$ is large at the wall and decreases with wall distance increasing the impact of the error in $\varepsilon_1$ on the diffusion term in the $\varepsilon$ equation.

An accurate value of $\varepsilon_1$ is important, as shown in Figure 9. Although $k_1$ from the look-up table differs from the wall integration value, $k$ approaches the wall integration solution away from the wall faster when Equation (3) is used for $\varepsilon$.

### 4.2. *Boundary condition for* $f$

In the original $v^2$-$f$ model (the model version with $N = 1$, see Appendix A) the non-dimensional variable $f^+$ has also a finite, non-zero value at the wall. Similarly to the proposed wall function



DOI: 10.1002/fld

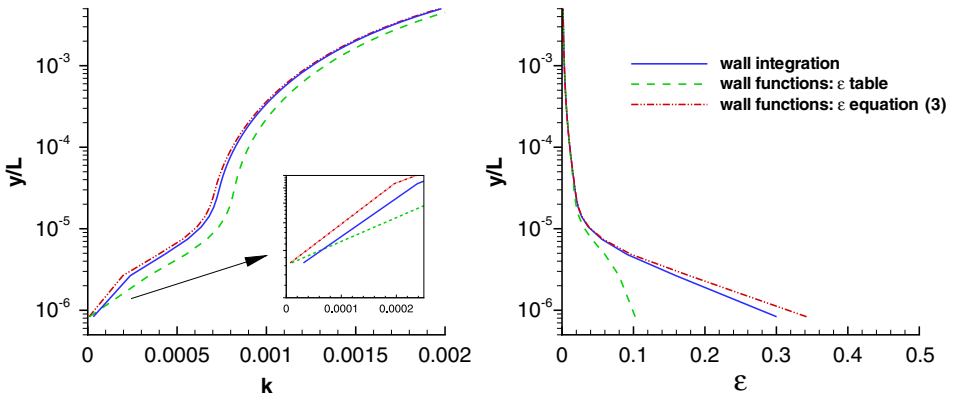


Figure 9. $k$ and $\varepsilon$ profiles at $x/L = 0.45$.

for $\varepsilon$ described above, a look-up table for $f$ in the first cell centre can be avoided by using the $\overline{v^2}$ equation:

$$kf = \frac{\overline{v^2}}{k}\varepsilon - \frac{\mathrm{d}}{\mathrm{d}y}\left((\nu + \nu_t)\frac{\mathrm{d}\overline{v^2}}{\mathrm{d}y}\right) \tag{4}$$

or in a discrete form using a finite difference method (with $\mathrm{d}\overline{v^2}/\mathrm{d}y = 0$ at the wall):

$$f_1 = \frac{\overline{v_1^2}}{k_1^2}\varepsilon_1 - \frac{1}{k_1}\frac{1}{y_{12}}\left((\nu + \nu_t)_{12}\frac{\overline{v^2}_2 - \overline{v^2}_1}{y_2 - y_1}\right) \tag{5}$$

where $\overline{v^2}_1$ and $k_1$ are obtained as before from the look-up table, $P_{k1}$ is computed using $(\mathrm{d}U/\mathrm{d}y)_1$ from the table and $\varepsilon_1$ from Equation (3). Note that close to the wall $y_{12}$ and $k_1$ are small and the factor in front of the bracket in Equation (5) becomes large amplifying the errors in the flux computation. In the viscous sublayer $\overline{v^2}$ increases with $y^4$ which may require a more accurate gradient approximation than the one used in Equation (5).

Coarse grid results for the flat plate computed using Equations (3) and (5) for $\varepsilon_1$ and $f_1$, respectively, are shown in Figure 10. The coarse grid results compare well with the results computed on a fine grid. In contrast to Figure 3, $f$ tends here to a non-zero value at the wall.

There is an interesting side effect of using wall functions with the $v^2$-$f$ model. It is well known that for $N = 1$ a coupled solver is needed due to strong coupling of the $\overline{v^2}$ and $f$ equations at the wall. The application of the proposed wall functions effectively decouples the variables and allows the use of a segregated solver.

## 5. FLOW OVER A RAMP

Incompressible flow over a two-dimensional ramp was studied experimentally in Reference [6], where a detailed experimental database was assembled for a range of Reynolds numbers (the intent was to study the effect of Reynolds number on the recirculation). The ramp is a circular arc with



DOI: 10.1002/fld

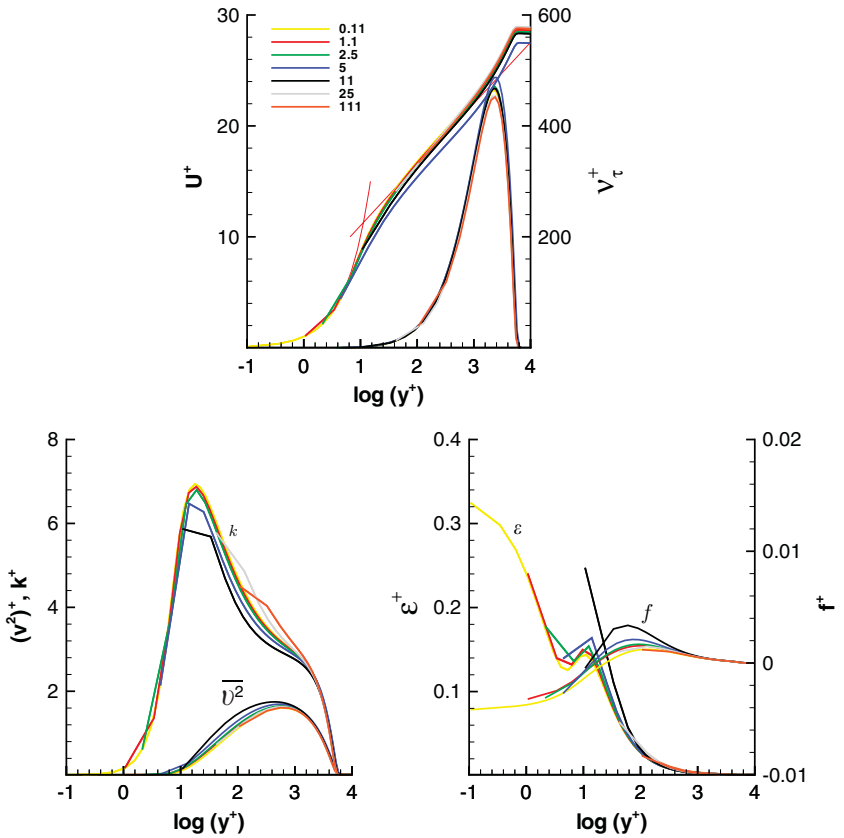


Figure 10. Application of adaptive wall functions using coarse grids for the original $v^2$-$f$ model, $N=1$.

the radius $R=1.814L$, where $L$ is the length of the ramp. The height of the ramp is $h=0.3L$ and the height of the channel upstream of the ramp is $H=1.871L$ (see Figure 11). The Reynolds number is $Re_L=U_\infty L/\nu=7\cdot 10^5$ and the momentum thickness based Reynolds number for the velocity profile at $x/L=-0.2$ is $Re_\theta=20\,100$.

Grids with the first cell centre $y^+$ of 1, 5, 17.5 and 30 in the channel upstream of the ramp were used. The grid size varies from $160\times 120$ cells for the finest grid to $160\times 80$ for the coarsest grid. Despite the constant size of the wall adjacent cells, the first cell centre $y^+$ varies significantly in the recirculation region, as shown in Figure 12. Convergence curves are shown in Figure 13. Note that the convergence is improved as the grid is coarsened.

Skin friction coefficient distribution is shown in Figure 14. As already discussed in Reference [2], even for recirculating flows the numerical solution in the near-wall region scales similarly to the flow over a flat plate—that is the reason why wall functions function for these flows (pressure gradient has a small effect). In addition, $y^+$ depends on $u_\tau$ and therefore the actual $y^+$ in the recirculation is much smaller than $y^+$ at the inflow on a given grid (e.g. it drops from 30 to 10). In the recirculation region as well as in the recovery region, the results with the coarsest grid ($y^+=30$) start to deviate from the other grids. Similar behaviour was also observed in the recirculation flow



DOI: 10.1002/fld

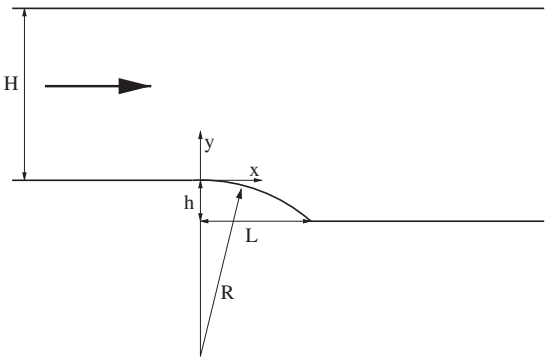


Figure 11. Ramp geometry.

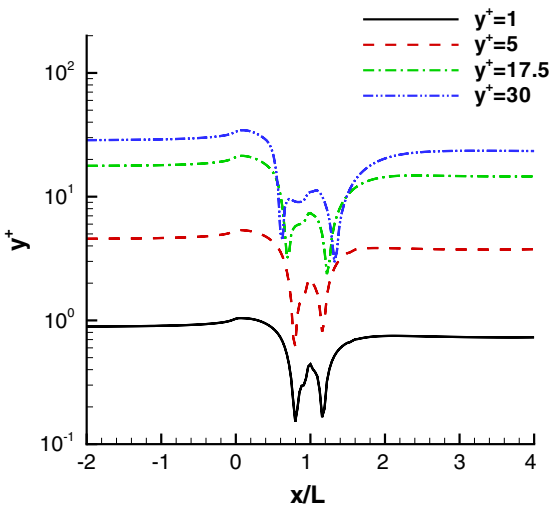


Figure 12. First cell centre $y^+$ distribution.

test case discussed in Reference [2]. It was attributed to the fact that $k$ in the recirculation region starts to deviate from the universal solution at lower $y^+$ values than the velocity. Curiously, the recirculation length computed with the $v^2$-$f$ model on the wall integration grid is significantly smaller than the experimental data, while the results on the coarser grids show a better agreement, see Table I.

Profiles of the velocity, $U$, and turbulent shear stress, $\tau_{xy} = \nu_t \, \mathrm{d}U/\mathrm{d}y$, non-dimensionalized using the velocity at the boundary layer edge $U_0$, are shown in Figures 15 and 16 for selected stations. The station $x/L = -2.0$ is located upstream of the ramp, $x/L = 0.0$ at the beginning of the ramp, $x/L = 1.37$ at the measured reattachment point and $x/L = 4.0$ downstream of the ramp (see Figure 14 for the location of measurement stations). At the first two stations the velocity and turbulent shear stress are very similar for all computations, i.e. the boundary layer thickness is well captured on all grids. However, all computations fail to predict the near-wall peak of the shear



DOI: 10.1002/fld

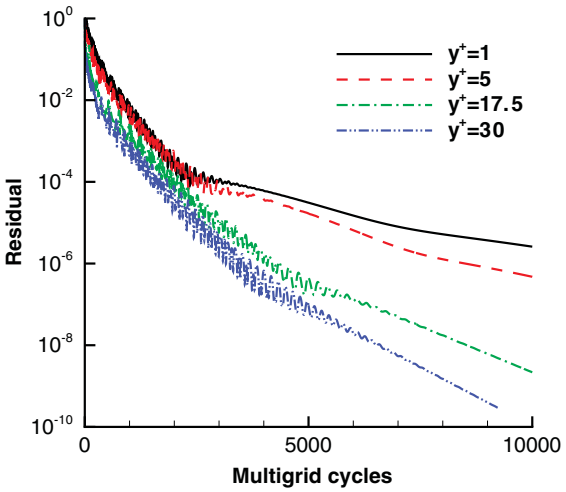


Figure 13. Convergence of the velocity residual.

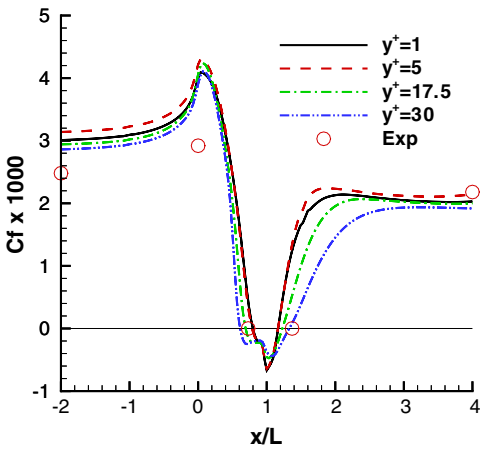


Figure 14. Skin friction coefficient.

Table I. Separation length and reattachment location.

| Grid | Separation length $(x/L)$ | Reattachment location $(x/L)$ |
|---|---|---|
| $y^+ = 1$ | 0.33 | 1.16 |
| $y^+ = 5$ | 0.36 | 1.16 |
| $y^+ = 17.5$ | 0.51 | 1.22 |
| $y^+ = 30$ | 0.69 | 1.32 |
| Experiment | 0.73 | 1.37 |



DOI: 10.1002/fld

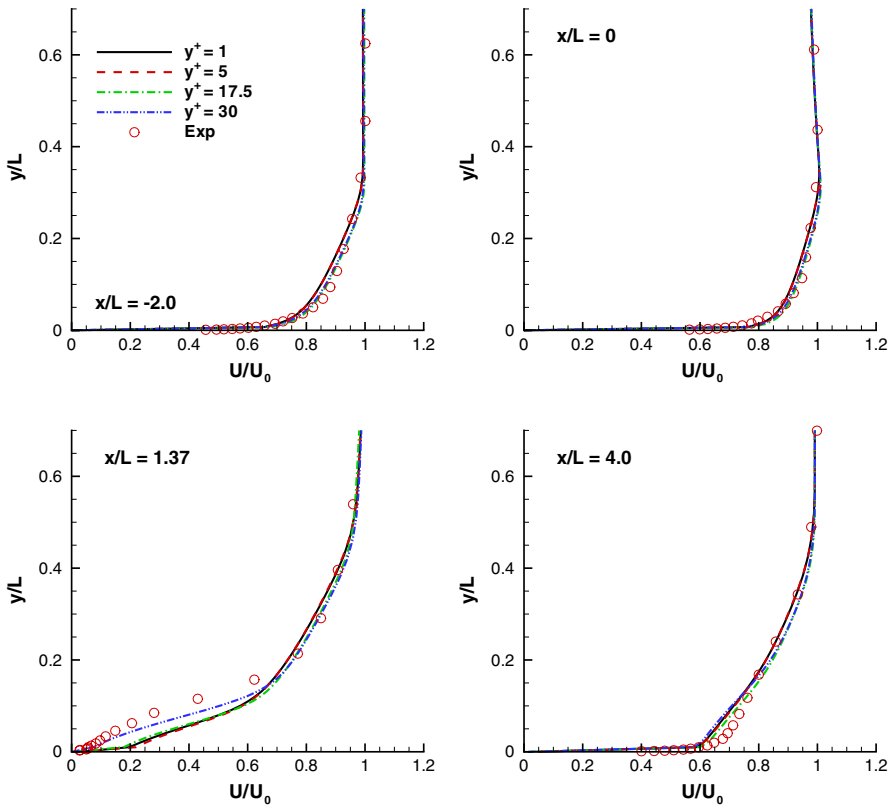


Figure 15. Velocity profiles.

stress. At the reattachment point, the prediction of the velocity and shear stress profiles become grid dependent. At the furthest downstream location the results are again less grid dependent, as the flow recovers to a standard zero pressure boundary layer.

To examine in more detail why the wall functions are not failing in the recirculation region, the wall integration solution is compared to the universal solution for the flat plate. This is done to assess the validity of the boundary condition provided by the look-up tables. The tangential velocity profiles (in non-dimensional form) in the recirculation region at $x/L = 1.0$ (dot-dot-dashed line) and downstream of the reattachment point at $x/L = 1.2$ (dashed line) computed on the wall integration grid are presented on the left in Figure 17. The profiles are compared with the universal solution (solid line). For $x/L = 1.0$ the universal solution has been plotted for reversed flow. The symbols in the same figure represent the tangential velocity $U_1^+$ and wall distance $y_1^+$ at the cell centre of the wall adjacent cell (diamonds for $x/L = 1.0$ and circles for $x/L = 1.2$) for the four coarser grids used (the four grids have a $y^+$ of 1, 5, 17.5 and 30 at the inlet of the domain). The plot shows, that although the flow is reversed at $x/L = 1.0$, the velocity profile follows the universal solution for small values of $y^+$ and a boundary condition for the coarse grids derived from the universal solution is a reasonable choice. At $x/L = 1.2$ (closer to the reattachment point) the discrepancy is more significant.



DOI: 10.1002/fld

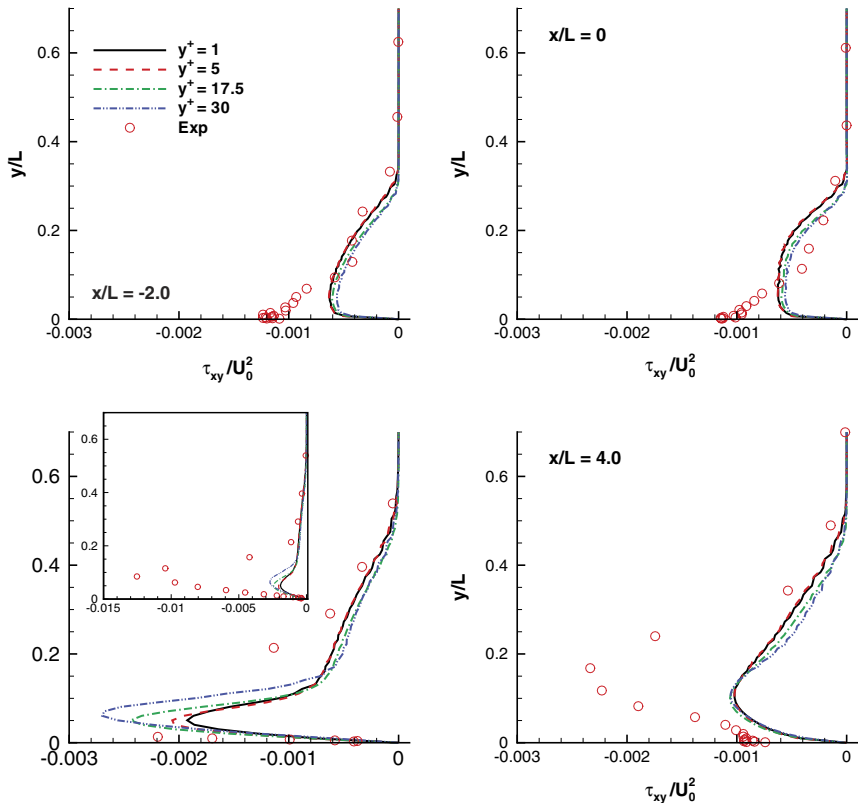


Figure 16. Turbulent shear stress profiles.

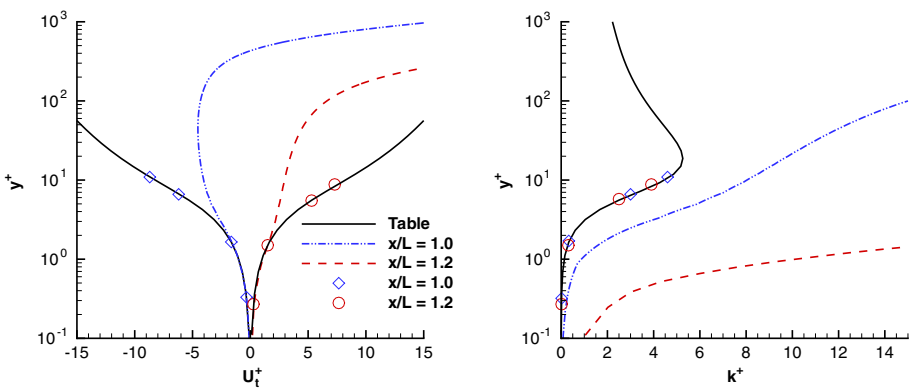


Figure 17. Profiles of tangential velocity $U_t^+$ and $k^+$ in the recirculation region.

The profiles of turbulent kinetic energy, $k^+$, differ more significantly from the look-up table. This can be attributed to high levels of $k$ generated in the separation region and convected downstream. In Figure 18, the streamlines for the solution computed on the finest grid ($y^+ = 1$) are overlayed



DOI: 10.1002/fld

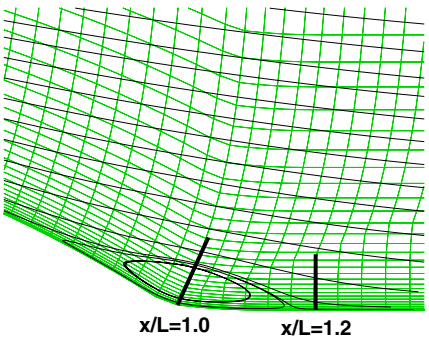


Figure 18. Streamlines computed on the finest grid ($y^+ = 1$) overlayed over the coarsest grid ($y^+ = 30$).

over the coarsest grid ($y^+ = 30$). The resolution is still sufficient for the recirculation region to be captured accurately.

## 6. CONCLUSIONS

This paper presents adaptive wall functions for the $v^2$-$f$ model. The wall functions are based on look-up tables created for the flow over a flat plate with zero pressure gradient. The inconsistency observed in Reference [2] for the $\varepsilon$ wall function when used for recirculating flows has been further investigated and a new boundary condition is proposed. A similar treatment for the variable $f$ is proposed for the $v^2$-$f$ model with $N = 1$.

The adaptive wall functions were applied to the flow over a ramp, where a recirculation region is present. In contrast to earlier computations this case has an additional complexity of curved solid walls. The results show that the wall functions allow accurate coarse grid computations with the $v^2$-$f$ model. It has also been observed that turbulence quantities deviate more significantly from the universal solution in the recirculation and recovery region.

## APPENDIX A: $v^2$-$f$ TURBULENCE MODEL

There are two versions of the $v^2$-$f$ model that are commonly used. They can be distinguished by the coefficient $N$ which affects the balance of terms in the $\overline{v^2}$ and $f$ equations. In the original model [3], this coefficient is equal to 1 and in the modified version [7, 8] it is set to 6. Setting the coefficient $N$ to 6 leads to zero wall boundary conditions for $f$. This modification was introduced to remove numerical difficulties that arise in the original model due to strong coupling of $f$ and $\overline{v^2}$ at the wall, see Equation (A8).

The $v^2$-$f$ model consists of three transport and one elliptic relaxation equations. The equation for turbulent kinetic energy, $k$, is

$$\partial_t(\rho k) + \nabla \cdot (\rho U k) = \rho P_k - \rho\varepsilon + \nabla \cdot ((\mu + \mu_t)\nabla k) \tag{A1}$$



DOI: 10.1002/fld

where

$$\rho P_k = R : \nabla U = -\tfrac{2}{3}\rho k(\nabla \cdot U) + 2\mu_t |S|^2 - \tfrac{2}{3}\mu_t (\nabla \cdot U)^2 \tag{A2}$$

with $S_{ij} = \frac{1}{2}(\partial_j U_i + \partial_i U_j)$ and $\mu_t$ being the eddy viscosity. The term $R : \nabla U$ is the inner product defined as $\sum_{ij} R_{ij} \nabla_i U_j$.

The equation for the dissipation of turbulent kinetic energy, $\varepsilon$, is

$$\partial_t(\rho\varepsilon) + \nabla \cdot (\rho U \varepsilon) = \frac{C_{\varepsilon 1}\rho P_k - C_{\varepsilon 2}\rho\varepsilon}{T} + \nabla \cdot \left( \left( \mu + \frac{\mu_t}{\sigma_\varepsilon} \right) \nabla \varepsilon \right) \tag{A3}$$

The equations for $k$ and $\varepsilon$ are supplemented with the equation for $\overline{v^2}$:

$$\partial_t(\rho\overline{v^2}) + \nabla \cdot (\rho U \overline{v^2}) = \rho k f - \rho N \frac{\overline{v^2}}{k}\varepsilon + \nabla \cdot ((\mu + \mu_t)\nabla \overline{v^2}) \tag{A4}$$

with $f$ representing the non-local effects

$$f - L^2 \Delta f = (C_{f1} - 1)\frac{2/3 - \overline{v^2}/k}{T} + C_{f2}\frac{P_k}{k} + (N-1)\frac{\overline{v^2}}{kT} \tag{A5}$$

where the turbulence length scale $L$ is

$$L = C_L \max\left[ \min\left[ \frac{k^{3/2}}{\varepsilon}, \frac{k^{3/2}}{\sqrt{6}\,\overline{v^2} C_\mu |S|} \right], C_\eta \frac{\nu^{3/4}}{\varepsilon^{1/4}} \right] \tag{A6}$$

and the turbulence time scale $T$ is

$$T = \min\left[ \max\left[ \frac{k}{\varepsilon}, 6\sqrt{\frac{\nu}{\varepsilon}} \right], \frac{\alpha k}{\sqrt{6}\,\overline{v^2} C_\mu |S|} \right] \tag{A7}$$

with $\alpha = 0.6$. The eddy viscosity is defined as $\mu_t = C_\mu \rho \overline{v^2} T$.

For solid walls, when $y \to 0$, this yields:

$$k(0) = 0, \quad \overline{v^2}(0) = 0, \quad \varepsilon \to \frac{2\nu k}{y^2}, \quad f \to -\frac{4(6-N)\nu^2 \overline{v^2}}{\varepsilon y^4} \tag{A8}$$

For the modified model ($N = 6$) the variable $f$ is zero at the wall.

The coefficients for the original version ($N = 1$) are:

$$\begin{aligned} &C_\mu = 0.19; \quad C_{\varepsilon 1} = 1.3 + 0.25/[1 + (0.5 C_L d/L)^2]^4; \quad C_{\varepsilon 2} = 1.9 \\ &C_{f1} = 1.4; \quad C_{f2} = 0.3; \quad C_L = 0.3; \quad C_\eta = 70; \quad \sigma_\varepsilon = 1.3 \end{aligned} \tag{A9}$$

and the coefficients for the modified version ($N = 6$) are:

$$\begin{aligned} &C_\mu = 0.22; \quad C_{\varepsilon 1} = 1.4(1 + 0.050\sqrt{k/\overline{v^2}}); \quad C_{\varepsilon 2} = 1.9 \\ &C_{f1} = 1.4; \quad C_{f2} = 0.3; \quad C_L = 0.23; \quad C_\eta = 70; \quad \sigma_\varepsilon = 1.3 \end{aligned} \tag{A10}$$



DOI: 10.1002/fld

## APPENDIX B: WALL FUNCTION TABLES

The wall function tables used in this paper were created for profiles of the non-dimensional velocity and turbulence variables obtained from a computation of flow over a flat plate with zero pressure gradient at a sufficiently large Reynolds number ($Re_\theta > 5000$) on a fine, wall-integration grid. The tables consists of the coefficients for cubic splines which approximate the profiles dependent on the non-dimensional wall distance $y^+$ (note that the velocity profile is stored as a function of the Reynolds number $Re = y^+U^+$; see Section 2).

Each spline extends from one cell centre to the adjacent cell centre of the fine grid. It has the form: $s(y^+) = a_0 + a_1 y^+ + a_2 y^{+2} + a_3 y^{+3}$. The coefficients are determined by enforcing the variable value and its gradient at the boundary points of each spline. The gradients are determined numerically from the profiles with a second order difference formula. There is no spline between the first and second data point since the first point is needed for the gradient computations. Viscous sublayer approximations are used between the wall and the first spline (see Reference [2]).

ACKNOWLEDGEMENTS

This research was sponsored by the Department of Energy through the ASC program at CITS, Stanford and by General Electric Aircraft Engines through the U.S.A. program.

REFERENCES

1. Launder BE, Spalding DB. The numerical computation of turbulent flows. *Computer Methods in Applied Mechanics and Engineering* 1974; **3**(3):269–289.
2. Kalitzin G, Medic G, Iaccarino G, Durbin PA. Near-wall behavior of RANS turbulence models and implications for wall functions. *Journal of Computational Physics* 2005; **204**(1):265–291.
3. Durbin PA. Separated flow computations with the $k$-$\varepsilon$-$\overline{v^2}$ model. *AIAA Journal* 1995; **33**:659–664.
4. Kalitzin G, Iaccarino G. Toward immersed boundary simulations of high-Reynolds number flows. *CTR Annual Research Briefs* 2003; 369–378.
5. van der Weide E, Kalitzin G, Schluter J, Alonso JJ. Unsteady turbomachinery computations using massively parallel platforms. *AIAA Paper 2006-0421*, 2006.
6. Song S, DeGraaff DB, Eaton JK. Experimental study of a separating, reattaching, and redeveloping flow over a smoothly contoured ramp. *International Journal of Heat and Fluid Flow* 2000; **21**(5):512–519.
7. Lien FS, Durbin PA. Non-linear $k$-$\varepsilon$-$\overline{v^2}$ modeling with application to high lift. *Proceedings of the Summer Program*, Stanford University, 1996.
8. Lien FS, Kalitzin G. Computations of transonic flows with the $v^2$-$f$ turbulence model. *International Journal of Heat and Fluid Flow* 2001; **22**:53–61.



DOI: 10.1002/fld